Unified Descriptor for Enhanced Critical Heat Flux during Pool Boiling of Hemi-wicking Surfaces

*Youngsup Song, Lenan Zhang, Carlos D. Díaz-Marín, Samuel S. Cruz, Evelyn N. Wang**

Department of Mechanical Engineering, Massachusetts Institute of Technology, Cambridge, MA 02139, USA

KEYWORDS

Critical heat flux, Roughness, Wettability, Capillary wicking, Phase change heat transfer

ABSTRACT

Boiling heat transfer is dictated by interfacial phenomena at the three-phase contact line where vapor bubbles form on the surface. Structured surfaces have shown significant enhancement in critical heat flux (CHF) during pool boiling by tailoring interfacial phenomena. This CHF enhancement has been primarily explained by two structural effects: roughness, which extends the contact line length at the bubble base, and wickability, the ability to imbibe liquid through surface structures by capillary pumping. In this work, we show that CHF enhancement on structured surfaces cannot be described by roughness or wickability alone. This result was confirmed using systematically designed micropillar surfaces with controlled roughness and wickability. Further,

we performed a scaling analysis and derived a unified descriptor, which represents the combined effects of thin film density and volumetric wicking rate. This unified descriptor shows a reasonable correlation with CHF values with our experiments and literature data. This work provides important insights in understanding the role of surface structures on CHF enhancement, thereby providing guidelines for the systematic design of surface structures for enhanced pool boiling heat transfer.

1. INTRODUCTION

Boiling is a vital process used to transfer heat effectively via harnessing the large latent heat of vaporization for a variety of energy applications. A major boiling parameter of interest is the critical heat flux (CHF, q''_{CHF}), the amount of heat that can be transferred over a specific area before exceeding the operational limit. Above CHF, a transition from the nucleate boiling to film boiling known as the boiling crisis occurs. During this process, coalesced vapor bubbles form a vapor film that becomes a dominant thermal resistance and can lead to thermal runaway resulting in catastrophic failure of systems.

Enhancing CHF, therefore, has been widely investigated to extend the operational limit and allow for larger safety margins for boiling systems [1, 2], by engineering boiling surface structures, e.g., micropillar, microchannel, microridge, and nanowire [3-7]. Meanwhile, fundamental understanding of the mechanism for enhanced CHF on such structured surfaces has been a subject of debate for over half a century. A force balance model on a static bubble, for example, attributes the CHF enhancement on structured surfaces to the augmented three-phase contact line length along the structures [3]. This static force balance model proposes surface

roughness, r, the ratio of actual surface area to the projected area, as a key structural property determining CHF that shows a reasonable correlation with experimentally measured CHF values [3, 8]. Another major group of CHF models attributes the CHF enhancement to the improved liquid rewetting by capillary pumping through surface structures, i.e., wickability. Structured surfaces that exhibit capillary-induced wicking are referred to as hemi-wicking surfaces. This capillary-induced flow occurs when the critical contact angle of a structured surface, $\theta_c = \cos^{-1}[(1-\varphi)/(r-\varphi)]$, becomes larger than the intrinsic contact angle, θ, where φ is the solid fraction at the solid-liquid interface. Most previous wickability-based models express the CHF of a hemi-wicking surface as the sum of the flat surface CHF, $q"_{\text{flat}}$, and an additional evaporation heat flux from a wicked liquid, $q"_{\text{w}}$, i.e., $q"_{\text{CHF}} = q"_{\text{flat}} + q"_{\text{w}}$. In this case, $q"_{\text{w}}$ has been characterized by a separate experimental measurement such as capillary rise height [9], spreading or absorption of liquid droplets [10, 11], and volumetric wicking flux of a pendant droplet [12, 13]. In addition to CHF models based on the experimentally characterized $q"_{\text{w}}$, a semi-analytical CHF model has been proposed by characterizing the surface wickability using Darcy's law [4]. The model derived a property related to the surface wickability: $P_{\text{cap}}K_{\text{B}}$ that determines CHF values of hemi-wicking surfaces. Here P_{cap} is the capillary pressure and K_{B} is the effective permeability (a permeability that incorporates shear stress from the bottom surface).

While CHF models based on roughness and wickability show good agreement with the corresponding experimental data, neither r (Figure 1a) nor $P_{\text{cap}}K_{\text{B}}$ (Figure 1b) can provide a general correlation for CHF, if we combine the existing literature data on Si and SiO_2 hemi-wicking surfaces. Inconsistent surface preparation or different boiling characterization methods across the literature may partly explain the discrepancy among different data sets [14, 15]; nonetheless, the unclear correlations of CHF values with roughness or wickability suggest that a

single property, i.e., roughness or wickability, is insufficient to describe CHF values of hemi-wicking surfaces. Recently, wickability-based models have included the structural effects on evaporation [16, 17]. In particular, an analytical model has proposed that the competition between evaporation and wicking fluxes associated with a varying dry area determines the CHF [17]. This model provides an important insight into the structural effects on evaporation; however, the model is highly sensitive to empirical parameters that are difficult to measure, e.g., bubble base diameter, accommodation coefficient, and thin-film thickness. Apart from roughness and wickability, a few studies have suggested that the boiling crisis is a critical phenomenon associated with stochastic bubble interactions [18-23]. Specifically, a machine learning-aided analysis has revealed that fundamental boiling parameters, e.g., nucleation site density, bubble departure frequency, growth time, and bubble base radius, need to be taken into account for the stochastic bubble interactions and the resulting CHF [22]. The structural effects on those fundamental boiling parameters, however, need further investigation.

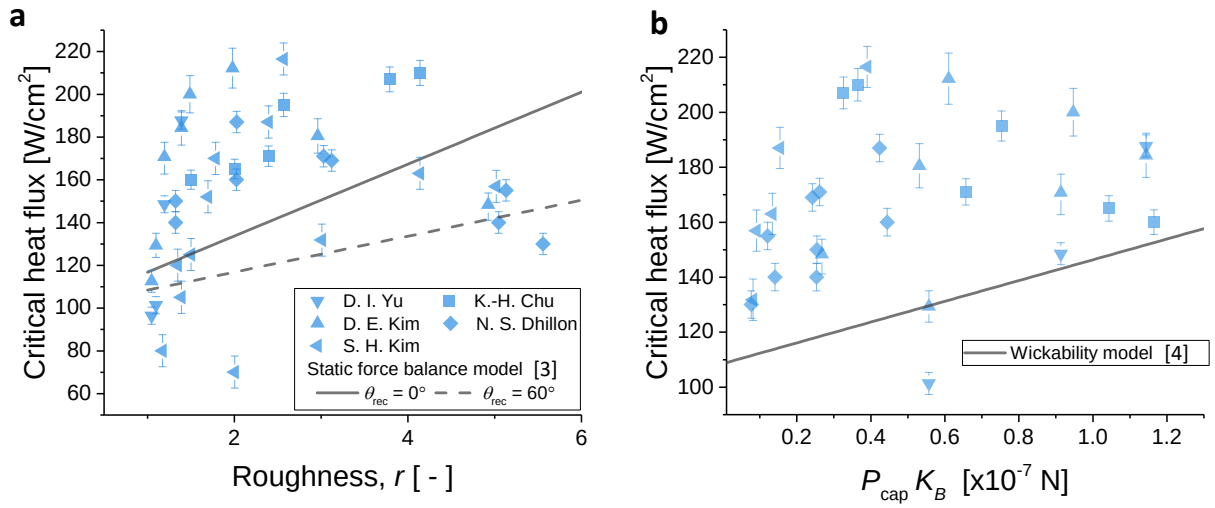

Figure 1. CHF data of hemi-wicking micropillar surfaces across the literature plotted with representative CHF models based on the (a) roughness r and (b) the product of capillary pressure and effective permeability $P_{cap}K_B$. The plots show no clear correlation between CHF values and r or $P_{cap}K_B$. Table S1 in the Supporting Information summarizes all of the data points in the plots.

In this work, we revisit the validity of previous roughness- and wickability-based CHF models using micropillar surfaces with systematically controlled roughness and wickability. By testing micropillar surfaces with a fixed roughness while varying wickability, and vice versa, we decoupled effects of each parameter on CHF values. Further, by leveraging our experimental results and previous visualization studies of boiling bubbles [18, 24, 25], we derived a unified descriptor using a scaling analysis. CHF values of our experiments and the literature data confirmed the scaling analysis. This work provides physical insights into the structural effects on

CHF, which can offer more general guidelines for the design of surface structures for high flux boiling applications.

2. DESIGN AND FABRICATION OF MICROPILLARS

Roughness is quantified as the ratio of actual surface area (A_{actual}) to projected area (A_{prj}) by $r = \frac{A_{\text{actual}}}{A_{\text{prj}}} = 1 + \frac{\pi dh}{p^2}$ for square micropillar arrays, where *d*, *h*, and *p* are the diameter, height, and pitch (pillar center-to-center distance) of micropillars (Figure 2a). Wicking performance is characterized as a product of the capillary pressure P_{cap} and the effective permeability K_{B} according to the previous semi-analytical model for CHF [4]. The capillary pressure is evaluated based on the liquid meniscus shape around micropillars that minimizes free energy: $P_{\text{cap}} = -\Delta E/\Delta V$, where ΔE and ΔV are the change in the free energy and volume due to the liquid filling into a unit cell of the micropillar array, respectively (detailed expressions appear in Section I of the Supporting Information) [17, 26]. We adopted the permeability correlation proposed by Yazdchi et al. [27], which combines the correlations developed by Gebart et al. [28] and Drummond and Tahir [29]. The permeability correlation proposed by Yazdchi et al., shows good agreement with experiments for the entire range of porosity ε [30], where the porosity is calculated as $\varepsilon = 1 - \frac{\pi d^2}{4p^2}$ for square micropillar arrays. Since this permeability *K* is developed for pillar arrays with unbounded top and bottom conditions, an additional term is required for our micropillar surfaces to account for the shear stress from the bottom surface. The effective permeability K_{B} accounting for viscous resistances from both the bottom surface and pillar

sidewalls, can be derived by solving the Brinkman equation with a no-slip condition at the bottom surface [17, 31].

$$K_{\mathrm{B}} = K\left[1 - \frac{\tanh(h\sqrt{\varepsilon/K})}{h\sqrt{\varepsilon/K}}\right]. \quad (1)$$

Detailed analysis on permeability is available in Section II of the Supporting Information [17, 27, 30]. Previous representative CHF models describe the CHF value as a function of either roughness or surface wickability. In fact, roughness and wickability depend on each other to some extent. For example, with the increase in the structural packing density, roughness generally increases, while liquid wicking speed increases and then decreases, leading to an optimal value due to the competition between capillary pressure and viscous resistance [26]. Therefore, decoupling the effect of roughness or wickability on CHF has not been straightforward. To investigate the decoupled effects of roughness and wickability on CHF values during pool boiling, we systematically designed a set of micropillar surfaces with varying r for a specific $P_{\mathrm{cap}}K_{\mathrm{B}}$, and vice versa. For example, we designed four different micropillar arrays with a similar $r\sim2.0$, while changing $P_{\mathrm{cap}}K_{\mathrm{B}}$ from 0.81×10^{-7} to 1.22×10^{-7} N (Sample #1, 2, 3, and 7). Likewise, we designed three different micropillar arrays with a similar $P_{\mathrm{cap}}K_{\mathrm{B}}$ value of $\sim 0.81 \times 10^{-7}$ N, while changing r from 1.5 to 3.0 (Sample #1, 4, and 5). In addition, a micropillar arrays with extremely high r but low $P_{\mathrm{cap}}K_{\mathrm{B}}$ was included to investigate a wider range of structural effects. Table 1 summarizes the dimensions and properties of all samples. We fabricated micropillar arrays through photolithography and deep reactive-ion etching (DRIE) processes on silicon wafers. At the end of the fabrication process, we etched away a C_4F_8 DRIE passivation layer by O_2 plasma and deposited a 60 nm SiO_2 layer over the entire surface by atomic layer deposition to ensure uniform hydrophilicity over the surface.

Details of the fabrication process are available in Section III of the Supporting Information. Figure 2 shows scanning electron microscopy (SEM) images of the fabricated micropillar arrays with the highest $P_{\mathrm{cap}}K_{\mathrm{B}}$ (Figure 2a, sample #3) and the highest r (Figure 2b, sample #6) among all samples.

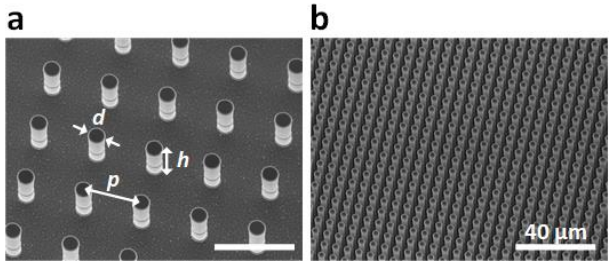

Figure 2. SEM images of micropillar arrays with dimensions of (a) d = 12 µm, p = 30 µm, h = 30 µm, and (b) d = 3 µm, p = 6 µm, h = 30 µm. The micropillar arrays in (a) and (b) have the highest $P_{\mathrm{cap}}K_{\mathrm{B}}$ and r, respectively, among seven different micropillar surfaces fabricated.

Table 1. Dimensions and properties of micropillar arrays. The roughness (r) and porosity (ε) are calculated as $r = 1 + \pi dh/p^2$ and $\varepsilon = 1 - \pi d^2/(4p^2)$, respectively. Two wicking properties are characterized, where $P_{\mathrm{cap}}K_{\mathrm{B}}$ and $P_{\mathrm{cap}}K_{\mathrm{B}}h$ are related to the speed of the wicking liquid front and volumetric wicking flow rate, respectively [17, 32].

Sample #	d [µm]	p [µm]	h [µm]	r [-]	ε [-]	$P_{\mathrm{cap}}K_{\mathrm{B}}$ [$\times 10^{-7}$ N]	$P_{\mathrm{cap}}K_{\mathrm{B}}h$ [$\times 10^{-12}$ N·m]
1	4	20	30	1.9	0.968	0.81	4.56
2	7	25	30	2.0	0.938	1.05	6.06
3	12	30	30	2.2	0.874	1.22	7.24
4	3	23	30	1.5	0.987	0.75	3.41
5	11	23	30	3.0	0.820	0.86	6.26
6	3	6	30	8.8	0.804	0.21	4.56

7	8	30	30	1.8	0.944	1.20	6.25

3. POOL BOILING MEASUREMENTS

We measured CHF values during pool boiling with high-purity deionized water by applying heat flux through a 100 nm-thick serpentine Pt heater (10×15 mm^2) deposited on the backside of each micropillar sample (12×18.5 mm^2). The Pt serpentine heater also served as a resistance temperature detector for the temperature characterization. We cleaned all samples with solvents (in the order of acetone, methanol, and isopropyl alcohol) followed by argon plasma before boiling to avoid unexpected alteration of CHF values by organic contaminants [14]. The pre-heated water was then introduced into the boiling chamber, which was degassed further by an immersion heater for 30 minutes before experimental measurements. We measured a voltage drop (V) and electric current (I) across the heater by gradually increasing the applied voltage up to the CHF point, where the heater resistance, i.e., sample temperature, drastically increased. The input heat flux was calculated as $q''_{\mathrm{in}} = (I \times V)/A_{\mathrm{h}}$, where A_{h} is the heating area of 10×15 mm^2. The bottom surface temperature was characterized by the resistance of heater, i.e., $R = V/I$, according to a pre-calibrated linear relationship between the resistance and temperature. Due to the slight size mismatch between the sample and heater, we numerically calibrated the experimentally measured data (COMSOL Multiphysics 5.3a) to account for the lateral heat spread across the sample. The details of the experimental setup and boiling characterization methods appear in Section IV of the Supporting Information.

For each micropillar geometry, we measured CHF values with two different samples. Figure 3 shows the average CHF values as a function of r and $P_{\mathrm{cap}}K_{\mathrm{B}}$. Our boiling results show

no clear correlation between CHF values and r and $P_{\mathrm{cap}}K_{\mathrm{B}}$, which confirms that the discrepancy between the literature data and previous CHF models (Figure 1) cannot be attributed to inconsistent surface conditions or boiling characterization methods across the literature only. Rather, the results directly show that CHF values on hemi-wicking surfaces cannot be described by either r or $P_{\mathrm{cap}}K_{\mathrm{B}}$ alone. Interestingly, however, CHF values generally increase with either r or $P_{\mathrm{cap}}K_{\mathrm{B}}$ when the other parameter is fixed, indicating that r and $P_{\mathrm{cap}}K_{\mathrm{B}}$ may have separate effects on CHF values. In Figure 3a, for example, the micropillar arrays with a similar r value ($r \approx 2$ for sample #1, 2, 3, and 7, colored in red) shows an increase in CHF values as $P_{\mathrm{cap}}K_{\mathrm{B}}$ increases except for one case (sample #7). Likewise, we found higher CHF values for micropillar arrays with higher r when $P_{\mathrm{cap}}K_{\mathrm{B}}$ remained similar ($P_{\mathrm{cap}}K_{\mathrm{B}} \approx 0.8 \times 10^{-7}$ N for sample #1, 4, and 5, colored in blue) as shown in Figure 3b.

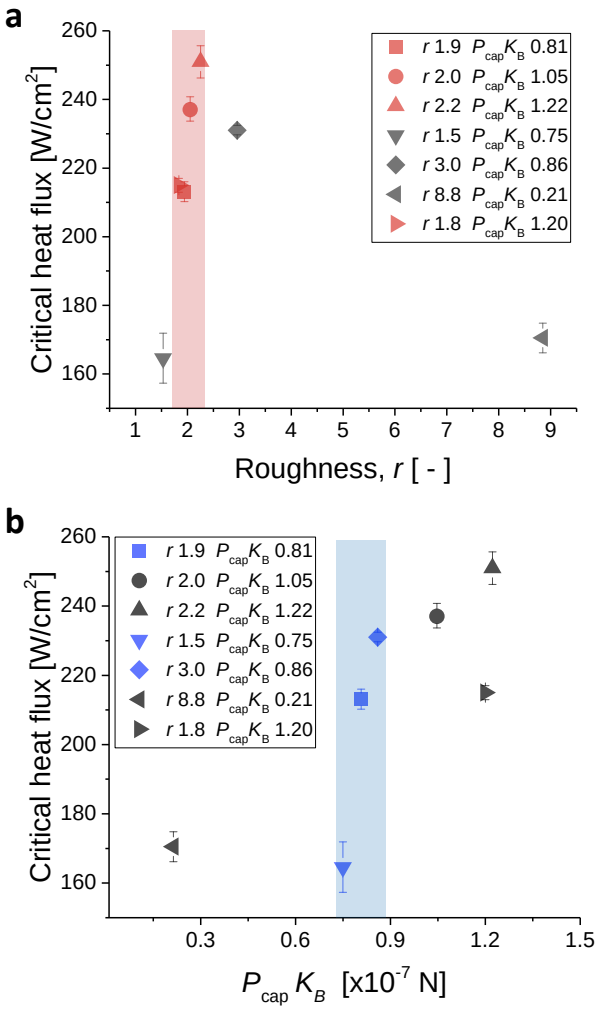

Figure 3. CHF values of micropillar arrays as a function of (a) r and (b) $P_{\mathrm{cap}}K_{\mathrm{B}}$. Data points show the average CHF values measured from two different samples for each pillar array. CHF values showed no clear correlation with both parameters. (a) For micropillar arrays with a similar r (colored in red), however, higher $P_{\mathrm{cap}}K_{\mathrm{B}}$ generally resulted in higher CHF values. (b) Likewise, higher r resulted in higher CHF values for micropillar arrays with a similar $P_{\mathrm{cap}}K_{\mathrm{B}}$ (colored in blue). The experimental measurement uncertainty was smaller than the marker size. The error bars were deviations of measurements on each sample from the average.

4. SCALING APPROACH

Although it is possible to understand the structural effects using a varying-dry-area model [17], this approach is highly sensitive to several empirical parameters such as bubble base diameter, accommodation coefficient, and thin-film thickness, which makes it challenging to directly assess the structural effects shown in our experiments. The detailed analysis on the varying-dry-area model is provided in Section V of the Supporting Information [17]. Alternatively, we applied a scaling approach to interpret our experimental results with minimal uncertainties from the empirical parameters. Considering that the contribution of convective heat transfer by single-phase liquid to the total boiling heat flux is insignificant near CHF [33, 34], CHF can be expressed as $q"_{\mathrm{CHF}} \approx \rho_{\mathrm{l}} h_{\mathrm{fg}} N" f V_{\mathrm{l,CHF}}$, where ρ_{l}, h_{fg}, $N"$, f, and $V_{\mathrm{l,CHF}}$ are the density of liquid, latent heat of vaporization, bubble nucleation site density, bubble departure frequency, and volume of evaporating liquid per bubble at CHF, respectively. Since structural dimensions of micropillars do not affect the nucleation site density significantly near CHF [16], we consider the nucleation site density roughly constant and scale the heat flux near CHF as $q"_{\mathrm{CHF}} \sim f V_{\mathrm{l,CHF}}$. The bubble departure frequency f describes how quickly bubbles nucleate and depart from a boiling surface. Specifically, if we assume bubbles depart at a characteristic volume V_{d}, at which buoyancy overcomes the surface tension force and drag force, V_{d} can be expressed as $V_{\mathrm{d}} = q"_{\mathrm{ev}} \frac{\tau_{\mathrm{d}} A_{\mathrm{b}}}{\rho_{\mathrm{v}} h_{\mathrm{fg}}}$, where $q"_{\mathrm{ev}}$, τ_{d}, A_{b}, and ρ_{v} are evaporation heat flux under a bubble, bubble departure period, bubble base area, and the density of vapor, respectively [35]. Assuming the thermophysical properties of water are constant, the departure frequency scales as $f = \frac{1}{\tau_{\mathrm{d}}} \sim q"_{\mathrm{ev}}$, i.e., surface structures with stronger evaporation can have higher bubble departure frequency. Given the high thermal conductivity of silicon, we can expect that dense micropillar

arrays may provide effective heat transfer for evaporation. In addition, when bubbles nucleate on micropillar surfaces (Figure 4a), the three-phase contact line pins at the top of micropillars and forms thin liquid films around the micropillars (Figure 4b – d). This thin film provides efficient heat transfer paths through their thin thickness (≤ 1 μm). Since the density of thin films (ξ) (shaded red regions in Figure 4b (top view) and 4c (cross-section view)) scales with the density of micropillars, i.e., $\xi \approx \frac{\pi d \delta_{\mathrm{tf}}}{p^2} \sim \frac{d\delta_{\mathrm{tf}}}{p^2}$, where δ_{tf} is the thin-film thickness threshold, the evaporation heat flux is expected to scale with the density of the thin film. Here the thin film density ξ is similar to roughness r, where both capture the structural packing density, but ξ is not dependent on the micropillar height. To confirm the scaling between the thin film density and evaporation heat flux, we modeled the thin-film evaporation in the unit cell of micropillar array (Figure 4c). The heat transfers from the boiling surface at the wall temperature (T_{w}) to the vapor bubble at the saturation temperature (T_{sat}) passing a silicon micropillar and bulk liquid water. Due to the orders of magnitude higher thermal conductivity of silicon ($k_{\mathrm{Si}} \approx 113\ \mathrm{W/(mK)}$ at 100 °C) than that of water ($k_{\mathrm{w}} \approx 0.68\ \mathrm{W/(mK)}$), we simplified the heat transfer path to be a one-dimensional resistance network including a micropillar and the surrounding thin liquid film. The conduction resistance through a micropillar is $R_{\mathrm{Si}} = \frac{4h}{\pi d^2 k_{\mathrm{Si}}}$. The thermal resistance of the thin liquid film can be calculated given the thin-film thickness profile, $\delta(z)$, along the distance from the micropillar top z as $R_{\mathrm{tf}} = \left[2k_{\mathrm{w}}\pi \int_{z_{\mathrm{ads}}}^{z_{\mathrm{tf}}} \frac{(\delta + \frac{d}{2})\sqrt{1+\left(\frac{d\delta}{dz}\right)^2}}{\delta} dz \right]^{-1}$ [36], where z_{tf} and z_{ads} are z values corresponding to thin-film thickness threshold (δ_{tf}) and non-evaporating adsorption layer thickness (δ_{ads}), respectively (Figure 4d). Here the thin-film thickness threshold and adsorption layer thickness are defined as 1 μm and 0.3 nm, respectively [37, 38]. The interfacial resistance

is estimated using the Schrage equation as $R_{\mathrm{int}} = \frac{1}{A_{\mathrm{int}}}\left(\frac{2-\chi}{2\chi}\right)\left(\frac{T_{\mathrm{v}} v_{\mathrm{lv}}}{h_{\mathrm{fg}}^2}\right)\left(\frac{2\pi \bar{R} T_{\mathrm{v}}}{\bar{M}}\right)^{1/2}\left(1-\frac{P_{\mathrm{v}} v_{\mathrm{lv}}}{2h_{\mathrm{fg}}}\right)^{-1}$, where A_{int} and χ are the thin-film interfacial area and accommodation coefficient, respectively. The accommodation coefficient is set to 0.03 in our calculations [39]. T_{v}, P_{v}, and v_{lv} are the vapor temperature, vapor pressure, and specific volume difference between the vapor and liquid phases, respectively. $\bar{R}$ is the universal gas constant ($8.314\ \mathrm{J/(molK)}$) and $\bar{M}$ is the molar mass of water ($0.01801\ \mathrm{kg/mol}$). The effective thermal resistance (R_{tot}) in one unit cell is then evaluated as $R_{\mathrm{tot}} = R_{\mathrm{Si}} + R_{\mathrm{tf}} + R_{\mathrm{int}}$, where the evaporation heat flux through one unit cell is $q"_{\mathrm{ev}} = \frac{T_{\mathrm{w}} - T_{\mathrm{sat}}}{R_{\mathrm{tot}} p^2}$. The additional details of the thin-film evaporation model and scaling are provided in Section V of the Supporting Information [36]. We evaluated $q"_{\mathrm{ev}}$ and ξ for micropillar arrays with a fixed height of 30 μm, while changing the pitch for pillar diameters of 5, 7, and 10 μm. The resulting plot of $q"_{\mathrm{ev}}$ normalized by the CHF value on a flat surface ($q"_{\mathrm{flat}} = 99.45\ \mathrm{W/cm^2}$) as a function of ξ (Figure 4e) monotonically increase while the derivative of the function decreases. Based on the shape of the curves, we scale the evaporation heat flux as $q"_{\mathrm{ev}} \sim \xi^{\mathrm{n}}$ with $0 < n < 1$. Note that we do not determine the value of the exponent *n* based on the modeling results, because the model depends on empirical parameters such as contact angle, accommodation coefficient, and thin-film thickness. Instead, we leave the exponent to be determined by the experimental results. Consequently, the departure frequency can be scaled to yield

$$f \sim q"_{\mathrm{ev}} \sim \xi^{\mathrm{n}}, \text{ where } 0 < n < 1 \qquad (2)$$

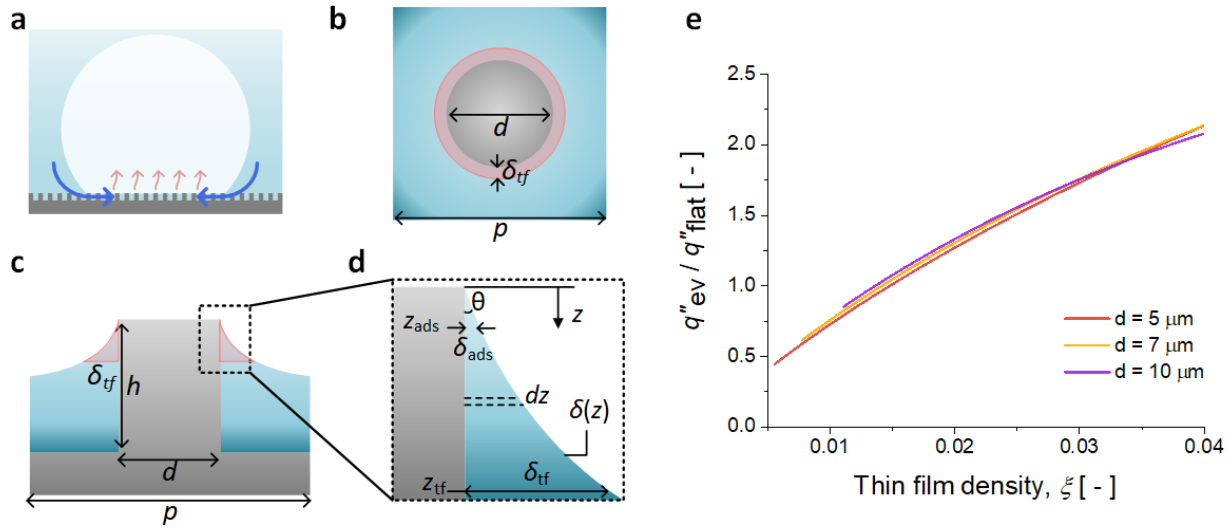

Figure 4. Structural effects on evaporation and rewetting under a boiling bubble on a hemi-wicking surface. (a) A schematic of a bubble nucleating on a hemi-wicking surface. Evaporation (red arrows) occurs from a liquid layer at the bubble base, while capillary-driven wicking (blue arrows) supplies the liquid from the circumference to the center of bubble base. (b) Top-view and (c) cross-sectional view schematics of thin-film evaporation in the unit cell of micropillar array. Shaded red area represents the thin-film region. (d) A magnified view of the thin-film region. (e) Evaporation heat flux normalized by the CHF value on a flat surface ($q"_{ev}/q"_{flat}$) as a function of thin film density, $\xi \sim \frac{d\delta_{tf}}{p^2}$. The plot shows an increase in evaporation heat flux with thin film density, i.e., $q"_{ev} \sim \xi^n$ with $0 < n < 1$.

Past synchrotron X-ray visualization of boiling bubbles on hemi-wicking surfaces has revealed that hemi-wicking surfaces maintain liquid layers under the boiling bubbles (as shown in Figure 4a) until a heat flux reaches CHF, where the bubble base dries out leading to the boiling crisis [25]. Combining this observation with stochastic bubble interaction models [18, 22], we presume

that hemi-wicking surfaces may delay the boiling crisis by maintaining a liquid layer under bubbles. Once the wicked liquid layer dries out, however, much more dry areas are suddenly created by the stochastic bubble interactions whereby the boiling crisis occurs. This capability of maintaining the liquid layer depends on the volumetric wicking flow rate. Therefore, we scale the volume of evaporating liquid per bubble at CHF ($V_{\mathrm{l,CHF}}$) as

$$V_{\mathrm{l,CHF}} \sim P_{\mathrm{cap}} K_{\mathrm{B}} h, \tag{3}$$

where $P_{\mathrm{cap}} K_{\mathrm{B}} h$ dictates the volumetric wicking flow rate of a hemi-wicking surface and h is the thickness of wicked liquid layer, i.e., micropillar height [32]. Note that there can be exceptional cases such as hemi-wicking surfaces with artificial cavities, e.g., microtube structures, where the extensive bubble coalescence due to high nucleation site density can limit the liquid supply, before capillary wicking becomes limiting, and trigger the boiling crisis [40]. Combining Equation (2) and (3), we obtain a unified descriptor of the CHF,

$$q''_{\mathrm{CHF}} \sim \xi^{\mathrm{n}} P_{\mathrm{cap}} K_{\mathrm{B}} h. \tag{4}$$

Figure 5a shows our CHF data as a function of the unified descriptor $\xi^{\mathrm{n}} P_{\mathrm{cap}} K_{\mathrm{B}} h$. The plot shows a clear positive correlation between our CHF data and $\xi^{\mathrm{n}} P_{\mathrm{cap}} K_{\mathrm{B}} h$, where n of 0.46 showed the best fit with our dataset (the sensitivity of n is discussed in Section VI of the Supporting Information). We also included literature data in Figure 5b using the same n, which confirms the positive linear relationship in a broader range. Here we included the literature data of silicon- and silicon dioxide-based hemi-wicking surfaces to investigate the sole effect of surface structure while excluding the effect of material properties. The exponent n, as previously discussed, depends on experimental and environmental parameters, so it may differ for different literature

data sets. This variation of n may lead a weaker correlation for the literature data set in Figure 5b compared than that of Figure 5a. Nonetheless, the improved correlation between CHF values with $\xi^{\mathrm{n}} P_{\mathrm{cap}} K_{\mathrm{B}} h$ (Figure 5) when compared to the correlations with r or $P_{\mathrm{cap}} K_{\mathrm{B}}$ alone (Figure 1) supports our scaling analysis; that is, the combined effect of thin film density and volumetric wicking rate affect CHF values by enhancing bubble departure frequency and delaying the growth of dry area, respectively. In fact, the scaling-derived descriptor $\xi^{\mathrm{n}} P_{\mathrm{cap}} K_{\mathrm{B}} h$ has the combined effects of previous roughness- and wickability-based models, which becomes more obvious by rearranging the parameters as $(\xi^{\mathrm{n}} h)(P_{\mathrm{cap}} K_{\mathrm{B}})$. Here $\xi^{\mathrm{n}} h$ is a parameter similar to roughness r, where their role to achieve enhanced CHF is essentially the extension of the contact line, and $P_{\mathrm{cap}} K_{\mathrm{B}}$ is the key parameter used in the wickability-based model. This result explains why the previous models could work for specific data sets. The roughness-based model could work when the effect of the extended contact line length was dominant, while the wickability-based model could work when the wickability effect was dominant.

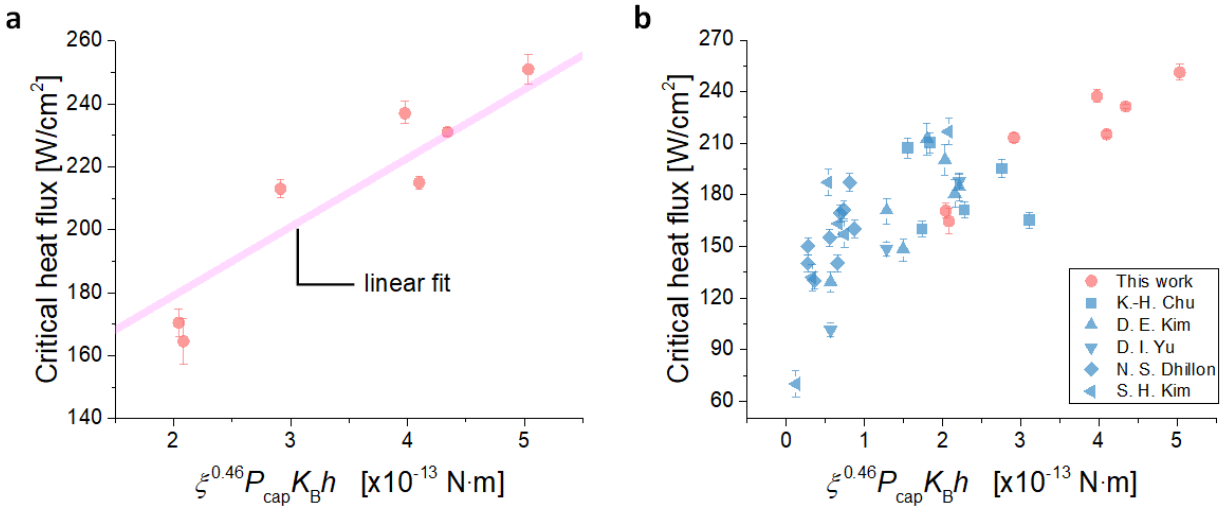

Figure 5. Experimentally measured CHF values versus $\xi^{0.46}P_{\mathrm{cap}}K_{\mathrm{B}}h$, where 0.46 is the exponent that fits best for our measurement. (a) CHF scaling results with our data and (b) including the literature data.

5. CONCLUSIONS

In this work, we showed that existing CHF correlations which used roughness or wickability as a single descriptor were limited to specific data sets. To investigate the effects of roughness and wickability on CHF values independently, we designed micropillar arrays with a fixed r while varying $P_{\mathrm{cap}}K_{\mathrm{B}}$, and vice versa. The experimentally measured CHF values on those micropillar arrays showed that, although there were no clear correlations of CHF values with either r or $P_{\mathrm{cap}}K_{\mathrm{B}}$ overall, CHF values generally increased with either r or $P_{\mathrm{cap}}K_{\mathrm{B}}$ when the other was fixed. This result directly showed that CHF is not solely a function of either r or $P_{\mathrm{cap}}K_{\mathrm{B}}$; instead, each parameter has separate effects on CHF. To understand the structural effects on CHF values, we performed a scaling analysis to derive a relationship for CHF with a new unified descriptor, $q''_{\mathrm{CHF}}\sim\xi^{\mathrm{n}}P_{\mathrm{cap}}K_{\mathrm{B}}h$. Here ξ^{n} and $P_{\mathrm{cap}}K_{\mathrm{B}}h$ affect CHF values by promoting bubble departure frequency and delaying the expansion of dry area, respectively. The scaling analysis was confirmed with CHF values from our experiments and literature data. CHF values from our experiments showed a positive linear correlation with $\xi^{0.46}P_{\mathrm{cap}}K_{\mathrm{B}}h$, which also agreed with existing literature data. Our work elucidate the separate roles of thin film density and wickability in enhancing CHF values, which can enable improved designs of boiling surfaces for a variety of high heat flux applications.

AUTHOR INFORMATION

Corresponding Author

*enwang@mit.edu

ACKNOWLEDGMENT

We appreciate the helpful discussion with Prof. Daniel J. Preston, Prof. Yangying Zhu, Prof. H. Jeremy Cho, and Dr. Zhengmao Lu on the limitations of previous models and the systematic design of micropillar surfaces. Y. Song acknowledges that the information, data, or work presented herein was funded in part by the Advanced Research Projects Agency-Energy (ARPA-E), U. S. Department of Energy, under Award Number DE-AR0000ABC. L. Zhang acknowledges support from the Singapore-MIT Alliance for Research and Technology (SMART) LEES Program. C. D. Díaz-Marín acknowledges the Air Force Office of Scientific Research under Grant No. FA9550-19-1-0392 with Dr. Ali Sayir as program manager, and a Professor Amar G. Bose Research Grant. S. S. Cruz acknowledges support from National Energy Technology Laboratory (NETL) of the U.S. Department of Energy with Richard Dunst as project manager. This work was performed in part at the Harvard University Center for Nanoscale Systems (CNS); a member of the National Nanotechnology Coordinated Infrastructure Network (NNCI), which is supported by the National Science Foundation under NSF award no. ECCS-2025158.

Highlights

- Experimentally demonstrated that pool boiling CHF enhancement on hemi-wicking surfaces cannot be explained by roughness or wickability alone.
- Experimental results of systematically designed micropillar surfaces showed that CHF depends on both roughness and wickability.
- Performed a scaling analysis to derive a relationship for CHF with a unified descriptor associated with thin film density and volumetric wicking rate.
- Thin film density and volumetric wicking rate enhance CHF by accelerating bubble departure frequency and delaying the dry-out at bubble base.
- CHF values from our experiments and literature data showed a positive linear correlation with the unified descriptor.

REFERENCES

[1] N.E. Todreas, M.S. Kazimi, Nuclear systems volume i: Thermal hydraulic fundamentals, third edition, CRC Press, 2021.

[2] J. Buongiorno, Can corrosion and crud actually improve safety margins in lwrs?, Ann. Nucl. Energy, 63 (2014) 9-21, http://www.sciencedirect.com/science/article/pii/S0306454913003745.

[3] K.-H. Chu, R. Enright, E.N. Wang, Structured surfaces for enhanced pool boiling heat transfer, Appl. Phys. Lett., 100(24) (2012) 241603, https://doi.org/10.1063/1.4724190.

[4] N.S. Dhillon, J. Buongiorno, K.K. Varanasi, Critical heat flux maxima during boiling crisis on textured surfaces, Nat. Commun., 6 (2015) 8247, http://dx.doi.org/10.1038/ncomms9247.

[5] D.I. Shim, G. Choi, N. Lee, T. Kim, B.S. Kim, H.H. Cho, Enhancement of pool boiling heat transfer using aligned silicon nanowire arrays, ACS Appl. Mater. Interfaces, 9(20) (2017) 17595-17602, https://doi.org/10.1021/acsami.7b01929.

[6] A. Zou, D.P. Singh, S.C. Maroo, Early evaporation of microlayer for boiling heat transfer enhancement, Langmuir, 32(42) (2016) 10808-10814, https://doi.org/10.1021/acs.langmuir.6b02642.

[7] H. Kim, H.S. Ahn, H.J. Kwak, M.H. Kim, D.E. Kim, Boiling crisis controlled by capillary pumping and viscous friction: Liquid penetration length and dry spot diameter, Appl. Phys. Lett., 109(24) (2016) 243901, https://aip.scitation.org/doi/abs/10.1063/1.4971986.

[8] K.-H. Chu, Y. Soo Joung, R. Enright, C.R. Buie, E.N. Wang, Hierarchically structured surfaces for boiling critical heat flux enhancement, Appl. Phys. Lett., 102(15) (2013) 151602, https://doi.org/10.1063/1.4801811.

[9] H.D. Kim, M.H. Kim, Effect of nanoparticle deposition on capillary wicking that influences the critical heat flux in nanofluids, Appl. Phys. Lett., 91(1) (2007) 014104, https://doi.org/10.1063/1.2754644.
[10] H.S. Ahn, H.J. Jo, S.H. Kang, M.H. Kim, Effect of liquid spreading due to nano/microstructures on the critical heat flux during pool boiling, Appl. Phys. Lett., 98(7) (2011) 071908, https://doi.org/10.1063/1.3555430.
[11] B.S. Kim, H. Lee, S. Shin, G. Choi, H.H. Cho, Interfacial wicking dynamics and its impact on critical heat flux of boiling heat transfer, Appl. Phys. Lett., 105(19) (2014) 191601, https://doi.org/10.1063/1.4901569.
[12] H.S. Ahn, G. Park, J.M. Kim, J. Kim, M.H. Kim, The effect of water absorption on critical heat flux enhancement during pool boiling, Exp. Therm Fluid Sci., 42 (2012) 187-195, http://www.sciencedirect.com/science/article/pii/S0894177712001471.
[13] M.M. Rahman, E. Ölçeroğlu, M. McCarthy, Role of wickability on the critical heat flux of structured superhydrophilic surfaces, Langmuir, 30(37) (2014) 11225-11234, https://doi.org/10.1021/la5030923.
[14] Y. Song, L. Zhang, Z. Liu, D.J. Preston, E.N. Wang, Effects of airborne hydrocarbon adsorption on pool boiling heat transfer, Appl. Phys. Lett., 116(25) (2020) 253702, https://doi.org/10.1063/5.0012839.
[15] M. Može, M. Zupančič, I. Golobič, Investigation of the scatter in reported pool boiling chf measurements including analysis of heat flux and measurement uncertainty evaluation methodology, Appl. Therm. Eng., 169 (2020) 114938, https://www.sciencedirect.com/science/article/pii/S1359431119359459.
[16] D.E. Kim, D.I. Yu, S.C. Park, H.J. Kwak, H.S. Ahn, Critical heat flux triggering mechanism on micro-structured surfaces: Coalesced bubble departure frequency and liquid furnishing capability, Int. J. Heat Mass Transfer, 91 (2015) 1237-1247, https://www.sciencedirect.com/science/article/pii/S0017931015009126.
[17] H. Hu, J.A. Weibel, S.V. Garimella, A coupled wicking and evaporation model for prediction of pool boiling critical heat flux on structured surfaces, Int. J. Heat Mass Transfer, 136 (2019) 373-382, https://www.sciencedirect.com/science/article/pii/S0017931018342960.
[18] L. Zhang, J.H. Seong, M. Bucci, Percolative scale-free behavior in the boiling crisis, Phys. Rev. Lett., 122(13) (2019) 134501, https://link.aps.org/doi/10.1103/PhysRevLett.122.134501.
[19] P. Lloveras, F. Salvat-Pujol, L. Truskinovsky, E. Vives, Boiling crisis as a critical phenomenon, Phys. Rev. Lett., 108(21) (2012) 215701, https://link.aps.org/doi/10.1103/PhysRevLett.108.215701.
[20] T. Charignon, P. Lloveras, D. Chatain, L. Truskinovsky, E. Vives, D. Beysens, V.S. Nikolayev, Criticality in the slowed-down boiling crisis at zero gravity, Phys. Rev. E, 91(5) (2015) 053007, https://link.aps.org/doi/10.1103/PhysRevE.91.053007.
[21] K. Wang, C.-Y. Li, M. Pellegrini, N. Erkan, K. Okamoto, Extended development of a bubble percolation method to predict boiling crisis of flow boiling, Int. J. Heat Mass Transfer, 165 (2021) 120660, https://www.sciencedirect.com/science/article/pii/S0017931020335961.
[22] M. Ravichandran, G. Su, C. Wang, J.H. Seong, A. Kossolapov, B. Phillips, M.M. Rahman, M. Bucci, Decrypting the boiling crisis through data-driven exploration of high-resolution infrared thermometry measurements, Appl. Phys. Lett., 118(25) (2021) 253903, https://doi.org/10.1063/5.0048391.
[23] L. Zhang, R. Iwata, L. Zhao, S. Gong, Z. Lu, Z. Xu, Y. Zhong, J. Zhu, S. Cruz, K.L. Wilke, P. Cheng, E.N. Wang, Nucleation site distribution probed by phase-enhanced environmental

scanning electron microscopy, Cell Reports Physical Science, 1(12) (2020) 100262, https://www.sciencedirect.com/science/article/pii/S2666386420302848.
[24] S.H. Kim, G.C. Lee, J.Y. Kang, H.S. Park, M.H. Kim, A study of nucleate bubble growth on microstructured surface through high speed and infrared visualization, Int. J. Multiphase Flow, 95 (2017) 12-21, https://www.sciencedirect.com/science/article/pii/S0301932216306085.
[25] D.I. Yu, H.J. Kwak, H. Noh, H.S. Park, K. Fezzaa, M.H. Kim, Synchrotron x-ray imaging visualization study of capillary-induced flow and critical heat flux on surfaces with engineered micropillars, Science Advances, 4(2) (2018) e1701571, http://advances.sciencemag.org/content/4/2/e1701571.abstract.
[26] R. Xiao, R. Enright, E.N. Wang, Prediction and optimization of liquid propagation in micropillar arrays, Langmuir, 26(19) (2010) 15070-15075, http://dx.doi.org/10.1021/la102645u.
[27] K. Yazdchi, S. Srivastava, S. Luding, Microstructural effects on the permeability of periodic fibrous porous media, Int. J. Multiphase Flow, 37(8) (2011) 956-966, https://www.sciencedirect.com/science/article/pii/S0301932211001005.
[28] B.R. Gebart, Permeability of unidirectional reinforcements for rtm, J. Compos. Mater., 26(8) (1992) 1100-1133, https://doi.org/10.1177/002199839202600802.
[29] J.E. Drummond, M.I. Tahir, Laminar viscous flow through regular arrays of parallel solid cylinders, Int. J. Multiphase Flow, 10(5) (1984) 515-540, https://www.sciencedirect.com/science/article/pii/030193228490079X.
[30] S. Cho, R. Tummala, Y. Joshi, Capillary performance of micropillar arrays in different arrangements, Nanoscale and Microscale Thermophysical Engineering, 22(2) (2018) 97-113, https://doi.org/10.1080/15567265.2018.1431749.
[31] H.C. Brinkman, A calculation of the viscous force exerted by a flowing fluid on a dense swarm of particles, Flow, Turbulence and Combustion, 1(1) (1949) 27, https://doi.org/10.1007/BF02120313.
[32] T.P. Allred, J.A. Weibel, S.V. Garimella, A wettability metric for characterization of capillary flow on textured superhydrophilic surfaces, Langmuir, 33(32) (2017) 7847-7853, http://dx.doi.org/10.1021/acs.langmuir.7b01522.
[33] C. Gerardi, J. Buongiorno, L.-w. Hu, T. McKrell, Study of bubble growth in water pool boiling through synchronized, infrared thermometry and high-speed video, Int. J. Heat Mass Transfer, 53(19) (2010) 4185-4192, https://www.sciencedirect.com/science/article/pii/S0017931010002838.
[34] S.H. Kim, G.C. Lee, J.Y. Kang, K. Moriyama, H.S. Park, M.H. Kim, Heat flux partitioning analysis of pool boiling on micro structured surface using infrared visualization, Int. J. Heat Mass Transfer, 102 (2016) 756-765, https://www.sciencedirect.com/science/article/pii/S0017931016302162.
[35] H. Sakashita, A. Ono, Boiling behaviors and critical heat flux on a horizontal plate in saturated pool boiling of water at high pressures, Int. J. Heat Mass Transfer, 52(3) (2009) 744-750, https://www.sciencedirect.com/science/article/pii/S0017931008004365.
[36] T. Liu, M.T. Dunham, K.W. Jung, B. Chen, M. Asheghi, K.E. Goodson, Characterization and thermal modeling of a miniature silicon vapor chamber for die-level heat redistribution, Int. J. Heat Mass Transfer, 152 (2020) 119569, http://www.sciencedirect.com/science/article/pii/S0017931019359046.
[37] S. Adera, D. Antao, R. Raj, E.N. Wang, Design of micropillar wicks for thin-film evaporation, Int. J. Heat Mass Transfer, 101 (2016) 280-294, http://www.sciencedirect.com/science/article/pii/S0017931015314800.

[38] A. Chatterjee, J.L. Plawsky, P.C. Wayner, Disjoining pressure and capillarity in the constrained vapor bubble heat transfer system, Adv. Colloid Interface Sci., 168(1) (2011) 40-49, http://www.sciencedirect.com/science/article/pii/S000186861100039X.
[39] B. Paul, Compilation of evaporation coefficients, ARS Journal, 32(9) (1962) 1321-1328, https://doi.org/10.2514/8.6277.
[40] Y. Song, S. Gong, G. Vaartstra, E.N. Wang, Microtube surfaces for the simultaneous enhancement of efficiency and critical heat flux during pool boiling, ACS Appl. Mater. Interfaces, (2021), https://doi.org/10.1021/acsami.1c00750.